The following article has been submitted to/accepted by Journal of Applied Physics. After it is published, it will be found at https://doi.org/10.1063/5.0079006.

Persistent Near-Infrared Photoconductivity of ZnO Nanoparticles Based on Plasmonic Hot Charge Carriers

Mohammed A. Ibrahem [1*], Emanuele Verrelli [2], Fei Cheng[2], Ali M. Adawi [2*], Jean-Sebastien G. Bouillard [2*] and Mary O'Neill [3*]

[1] Laser Science and Technology Branch, Applied Sciences Department, University of Technology- Iraq.

[2] Department of Physics and Mathematics, University of Hull, Cottingham Road, Kingston upon Hull HU6 7RX, United Kingdom.

[3] School of Science and Technology, Nottingham Trent University, Clifton Lane, Nottingham NG11 8NS, United Kingdom.

mohammed.a.ibrahem@uotechnology.edu.iq, a.adawi@hull.ac.uk, j.bouillard@hull.ac.uk, and mary.oneill@ntu.ac.uk

Abstract

We report on the coupling of ZnO nanoparticles with plasmonic gold nanoislands in a solution processed photodetector, which results in a clear enhancement in the optical absorption and the electrical responsivity of ZnO nanoparticles to cover the visible and the near-IR (NIR) spectral range, well beyond its intrinsic optical absorption. This enhancement, which arises from the coupling between ZnO nanoparticles and the plasmonically mediated hot electron generation in the Au plasmonic nanoislands, results in a significant plasmonically driven photoresponse in the NIR of 2.5×10^{-5} A/W. The recorded photocurrent exhibits a persistent behaviour, which is attributed to surface defect states in the ZnO nanoparticles. This study provides a route to solution processed, low-cost device fabrication schemes with important implications on low processing temperature optoelectronics technology to enhance the performance of photovoltaic devices over a wide solar spectrum. Additionally, this unusual behaviour paves the way towards harnessing plasmonic resonances to probe and examine the surface defects of metal oxide semiconductors.

Keywords: *ZnO nanoparticles, Plasmonic photoconductivity, hot electrons, gold nanoislands*

1- Introduction

Solution processable semiconductors show promising optoelectronic features with highly scalable compatibility for the next generation of smart products, low-cost optoelectronic devices and medical sensors [1]. Solution processed ZnO shows a great potential due to its abundance, low cost, ease of processing and unique optical properties [2,3,4]. Consequently, there is an extensive literature on its ultraviolet photoconductivity (PC) [5].

However, photodetection of longer wavelengths of the optical spectrum, such as in the near-infrared (NIR), underpins a range of key applications ranging from free-space optical communication to chemical sensing and biomedical imaging [6,7,8]. This is usually achieved by complex systems involving costly compound material structures [9] such as GaAs, which renders photodetector fabrication, and their applications, expensive [10] and highly dependent on a limited number of foundries worldwide. Moreover, such detectors cover only a specific spectral range, mostly in the NIR, 1-2 μm, which makes them incompatible with low-cost manufacturing for multiwavelength photodetection systems.

On the other hand, solution-processed techniques have recently revolutionized the photodetector fabrication industry, enabling high performance, low cost and large-scale production to be viable without the need for complicated evaporation equipment [11,12]. ZnO, among other metal oxide semiconductors, is a material of choice for solution-processed photodetectors. It exhibits promising optoelectronic properties with superior chemical stability and photocorrosion resistance, while remaining a highly affordable and abundant material. On the other hand, due to its wide bandgap of 3.37 eV, ZnO photoexcitation is limited to the UV part of the spectrum, which greatly limits its applications in optoelectronic devices at longer wavelengths [13,14].

However, recent work has shown that the photoresponse of ZnO can be extended to cover the visible [15] and the near-infrared (IR) [16] by modifying the material's bandgap with either intrinsic doping, inherited in the ZnO nanostructures mainly by the fabrication process, or extrinsic doping by adding another material, or both [17,18], as well as through coupling to other materials, such as perovskite [19]. However, such processing techniques often lead to broad visible PC spectral ranges with spectral bandwidths of the order of 100 nm, therefore hindering their applications in imaging and photodetection devices.

In parallel, the generation of hot charge carriers by plasmonic nanostructures has recently gathered a large interest [20]. Plasmonic resonances can decay either via scattering into a photon, or via the excitation of electron-hole pairs with energy higher than the Fermi energy, which quickly thermalise through electron-electron scattering, giving rise to a Fermi-Dirac distribution corresponding to a much higher electron temperature. Subsequently, through collisions with the lattice, this extra energy is dissipated as heat in the material, corresponding to the commonly known Ohmic losses. In the few hundred to thousand femtoseconds before the electron temperature thermalises, the corresponding hot charge carriers can be used to drive photochemical or photocatalytic reactions [21,22], or create a photocurrent after tunnelling into the conduction band of a nearby semiconductor [23]. Such plasmonically generated hot-charge carriers have been used to enable sub-bandgap photoresponse over a wide spectral range, from the UV to the far-infrared [23,24]. Additionally, hot electrons injection has been found to be an effective strategy to enhance the electrical photoresponse of wide bandgap semiconductors below their optical band gaps [25,26,27].

Here, we demonstrate a NIR photoresponse from a vertical configuration photodetector device based on ZnO nanoparticles photosensitized by randomly distributed Au nanoislands, which are used to stimulate sub-bandgap photo-charge carriers in ZnO by hot electrons injection, arising from the decay of surface plasmons. The Au nanoislands allow to cover a spectrally broad near-infrared plasmonic resonance due to their inherent random shape and size, and represent a relatively fast and cost-effective method to create plasmonic nanostructures [28,29,30]. The unusual plasmonic behaviour observed here (persistent and relatively high PC) emphasizes the crucial role of surface defect states in such plasmonic photodetection devices.

2- Experimental method

Device fabrication

Two types of devices were fabricated following a simple vertical configuration structure: a plasmonic device and a reference device. The plasmonic device (shown in figure 2) incorporates Au nanoislands (ITO/PEDOT/Au/ZnO/Al) while the reference device has the same structure without Au nanoislands (ITO/PEDOT/ZnO/Al). All devices were built on pre-patterned 100 nm ITO fingers (20 Ω / square) evaporated on a 20 nm coating of SiO_2 (synthetic quartz) overlying a 20×15 mm^2 polished soda-lime, float glass substrate bought from Ossila. Each working device

consists of three ITO fingers, with each finger measuring 100 μm by 10 mm, all connected to a 2 mm wide ITO pad (figure S1 of the supporting information). Each substrate contains 8 working devices, which can be addressed individually by connecting a needle probe to the relevant ITO pad.

The substrates were cleaned thoroughly followed by UV/Ozone treatment for 3 min, to remove any organic and impurities remaining on the surface and to improve surface wettability. The devices were then fabricated by sequential spin-coating and thermal evaporation on the substrates. First, a 30 nm layer of PEDOT:PSS (poly(3,4-ethylene dioxythiophene) polystyrene sulfonate), (Ossila Ltd) was spin-coated in air at 2000 rpm for 30 sec followed by thermal annealing at 150 °C for 10 min in air. Then, a high purity gold thin film of thickness ≈25 nm was thermally evaporated on top of the PEDOT:PSS layer at a rate of 0.1 A/sec and under a pressure of 5×10^{-7} mbar using an HHV Auto 500 multifunctional evaporator. During the thermal evaporation, the devices were positioned approximately 30 cm from the gold crucible (on a rotating holder) inside the evaporation chamber to prevent any excess heating of the PEDOT:PSS layer. Finally, a 120 nm (± 5nm) layer of ZnO nanoparticles was deposited by spin-coating at 2000 rpm for 30 sec from a suspension of ZnO NPs (2.5 wt.%) in chloroform. The ZnO NPs solution was prepared in-house using literature methods with some modification. More information on the preparation method can be found in our publication [31]. This was followed by a final annealing at 150 °C in air for 10 min. The devices were then irradiated for 2 min by UV/Ozone to remove any organic ligands attached to the ZnO nanoparticles before evaporating a 150 nm thick Al back electrode.

Device characterisation

Photocurrent measurements were performed as a function of illumination wavelength using a high intensity, 150 W Xenon white light solar simulator (Abet Technologies, model 10500) as the light source, covering the wavelength range 400 nm to 1800 nm. The devices were irradiated from the ITO side. Narrow spectral bands were selected using a set of dielectric bandpass filters (Thorlabs) with 10 nm bandwidth (±3 nm) and central transmission wavelengths of 600 nm, 650 nm, 700 nm, 750 nm, 800 nm, 850 nm, 900 nm, and 950 nm. The photocurrent maximum for each wavelength was corrected for each filter's FWHM to account for any variation in the bandpass spectral width in the visible and near-IR. Optical absorption spectra were measured using a Thermo Scientific (EVOLUTION 220) spectrophotometer over the wavelength range 300 nm to 1000 nm. The

incident light intensity was measured using a digital compact power and energy meter console with calibrated photodiode sensors from Thorlabs (PM100D). The devices were irradiated with a normally incident light beam covering the whole device area.

The Atomic Force Microscopy (AFM) was recorded in tapping mode using TESP-V2 etched silicon probes (42N/m, 320 kHz, without reflecting coating to the back of the tip) on a Bruker Dimension Edge device with ScanAsyst. The surface profile of the Au nanoislands film was plotted using ImageJ software (1.51j8). I-V (current-voltage) and transient photocurrent measurements were recorded using two electrical needle probes connected to a 2400 Keithley source meter interfaced with a computer through the BenWin+ software.

3- Results and discussion

Device morphology and optoelectronic properties

Transmission electron microscopy (TEM) results (figure 1A) shows the crystalline structures of ZnO NPs with an average diameter of 12 nm. X-ray diffraction patterns (XRD) of ZnO NPs film, shown in figure 1B, confirming the wurtzite crystalline phase of ZnO NPs. The kinetics of Au nanostructures formation during the deposition process are strongly dependent on the atom-substrate interactions, inherently linked to the substrate nature, and are ultimately found to follow the Wolmer-Weber [32] film growth model, often leading to the formation of 3D Au nanoislands [33]. Consequently, the formation of well-defined Au nanoislands on PEDOT:PSS results from the molecular scale structures of the PEDOT:PSS surface composition,[34] which has been shown to hinder the diffusion of gold atoms on the surface and facilitate the gold nucleation process [33,35].

In this study, the Au nanoislands deposited on the PEDOT:PSS surface have a nominal thickness of 25 nm, measured with a calibrated QCM (quartz crystal monitor), and create plasmonic nanogaps with sizes ranging 10-50 nm (Figure 2A). A typical surface profile of the deposited Au nanoislands film deposited on top of PEDOT:PSS is shown in figure 2B. The effect of the Au nanoislands is clearly visible on the device extinction spectrum (Figure 3A), taken in transmission before evaporating the back-aluminium electrode, which clearly displays the characteristic broadband extinction peak between 600 nm and 900 nm. This optical response depends on the morphology of the nanoisland film (nanoislands size, shape and thickness) and can be tuned accordingly [36,37]. Six plasmonic substrates were prepared with identical preparation conditions,

all of which show a very good level of reproducibility, with the data collected from all devices showing a very good repeatability.

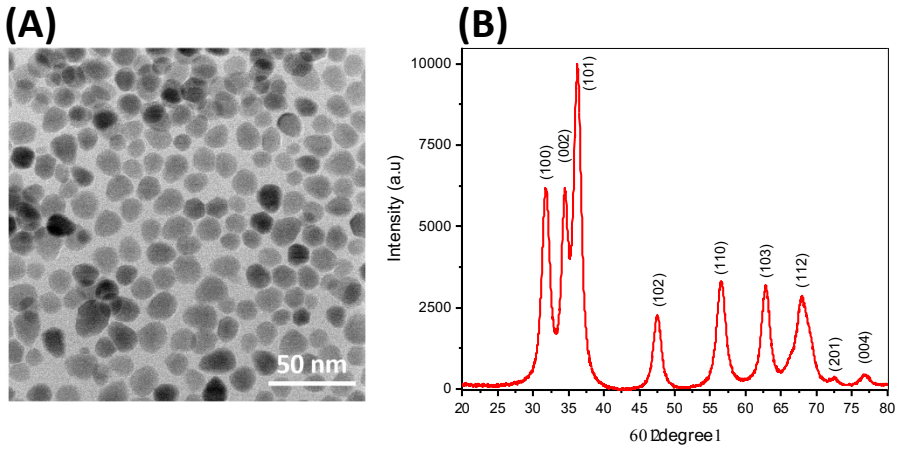

Figure 1: (A) TEM of the as prepared ZnO nanoparticles used in this work. (B) XRD of ZnO NPs powder showing the typical wurtzite crystalline structure.

Two device geometries were fabricated: plasmonic devices incorporating the Au nanoislands (ITO/PEDOT/Au/ZnO/Al), and a reference device with the same structure but without Au nanoislands (ITO/PEDOT/ZnO/Al) (Figure 2C).

In parallel with the device morphology, charge transfer between the various device layers directly impacts the optoelectronic properties of the device. Figure 2D illustrates the energy band diagram of the plasmonic device. The ZnO nanoparticles workfunction (4.3 eV) [38] results in the formation of an ohmic contact with the aluminium (Al) layer [38,39], and a p-n junction with the PEDOT:PSS layer [40]. On the other hand, since the gold workfunction is 5.1 eV, the interface between ZnO nanoparticles and the gold nanoislands corresponds to a Schottky junction, with a barrier height up to 1 eV depending on the junction quality and interface conditions [38]. This junction structure is supported by the dark I-V (current-voltage) measurements recorded for both the plasmonic and reference devices with different applied voltages polarity (figure S2 in the supporting information).

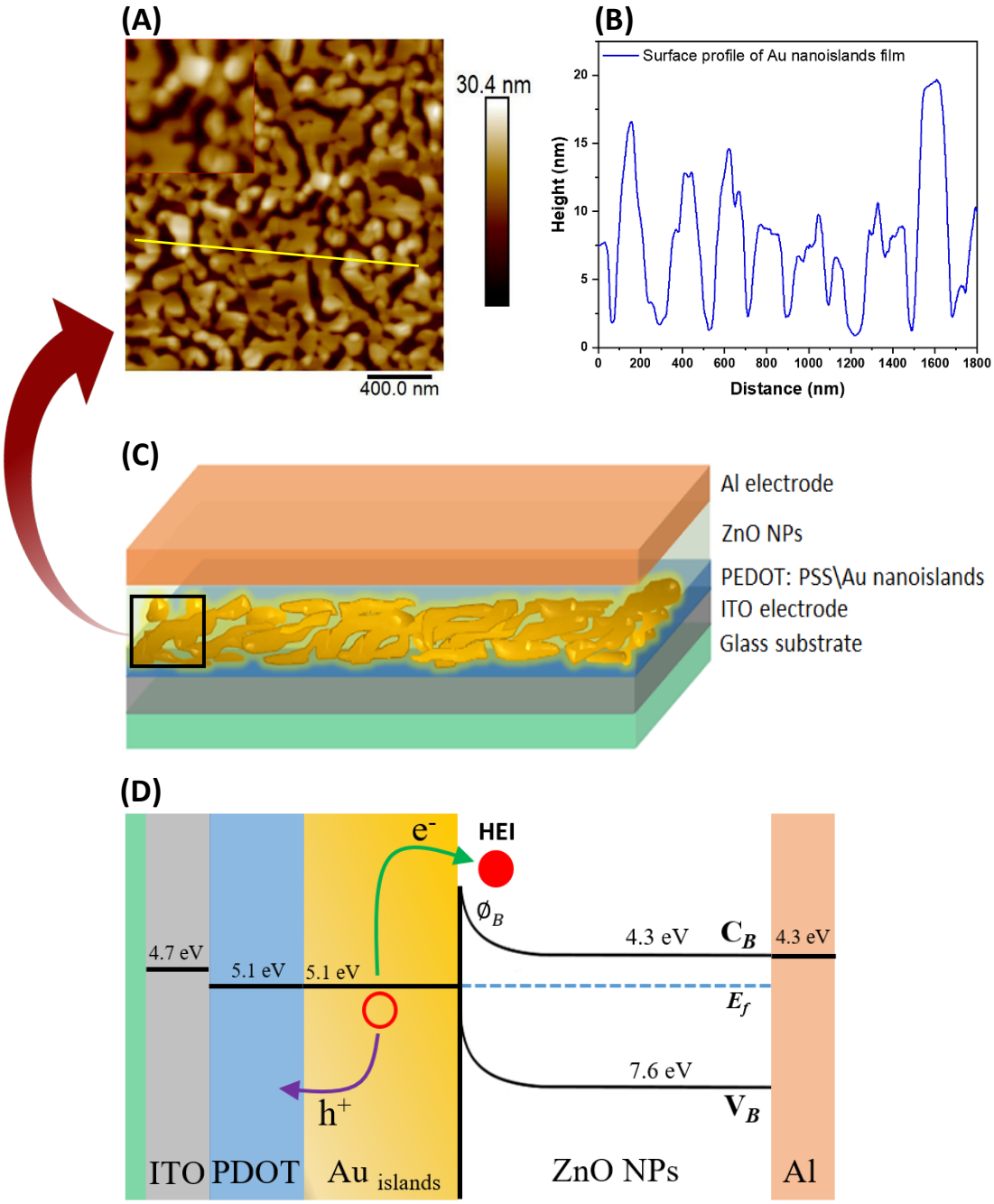

Figure 2: (A) AFM topography of gold nanoislands evaporated on top of PEDOT:PSS. The inset is a magnification image illustrating the nanogaps existing in the Au nanoislands film. The AFM inset image has a scale of 100 nm. (B) Surface profile of the Au nanoislands film, corresponding to the cross-section illustrated by a yellow line in the AFM image in (A). (C) A schematic representation of the plasmonic near-IR photodetector device incorporating gold nanoislands evaporated on top of a PEDOT:PSS layer. Each working device consists of three ITO fingers connected to the same ITO pad. (D) Energy band diagram showing the energy levels offset of the plasmonic device investigated in this work. The interface energies of ITO/PEDOT:PSS/Au/ZnO NPs/Al were based on references [41,38].

The optoelectronic properties of the reference device show no photocurrent in the probed visible-NIR region, 600-950 nm, with photon energies well below the ZnO bandgap. On the other hand, the plasmonic device displays a clear photocurrent in the wavelength range between 600 and 850 nm, peaking at 800 nm. Although corresponding to energies well below the ZnO bandgap energy, the absence of this photocurrent in the reference device and its spectral overlap with the plasmonic resonance of the Au nanoislands in the device (Figure 3A, Figure S3 A&B, supporting information) clearly indicate that it arises from the plasmonic hot charge carrier generation in the Au nanoislands.

In parallel, photocurrent values show a rapid decrease deviating from the absorption curve for irradiation at longer wavelengths, as shown in figure 3A. This sharp decrease is attributed to the lower photon energy at those wavelengths, which greatly decreases the probability for electrons to overcome the Schottky barrier between the gold and the ZnO NPs. The enhancement in the NIR photocurrent can be understood through Fowler theory which explains the efficiency of the hot electrons injection process from the metal to the semiconductor through the Schottky junction [42,43]. The efficiency of hot electron injection through the metal-semiconductor barrier is found to be affected by the nanostructuring of the plasmonic metal, which can ultimately lead to an enhancement of the injection process and a lowering of the barrier height [44,45]. Furthermore, when electrons can only be scattered at the metal-semiconductor interface, the momentum conservation requirement is found to be relaxed [46]. Under such conditions, Fowler's original expression for the hot electrons injection quantum yield (QY) can be rewritten as [47]: $QY_{(\omega)} = (\hbar\omega - E_B)/(2\hbar\omega)$, where $\hbar\omega$ is the photon excitation energy and E_B is the Schottky barrier height. Herein, we calculated the hot electron injection yield in the NIR utilizing the plasmonic absorption of our device as shown in figure 3B, S4. The reproduced photocurrent data (the efficiency of hot electron injection) supporting the experimentally measured plasmonic photocurrent is illustrated in figure 3A.

The NIR photocurrent of the plasmonic device was further investigated by illuminating the device under constant bias voltage with light of 850 nm wavelength and recording the photocurrent as a function of incident light power (Figure 3C, S5). The photocurrent values show an almost linear increase with incident light power, with minor deviations from the fitting line attributed to charge trapping in ZnO NPs [48], either through activation of charged traps or filling of empty traps.

The device responsivity can be derived from the photocurrent (Figure 3C), and shows that, in our plasmonic device, the responsivity decreases with increasing incident light power. This can be attributed to the electrons reimbursement process (charge balancing maintained by the PEDOT:PSS layer) by which hot electrons can be generated and sustained in the gold and injected in the ZnO [49,50].

The observed photocurrent responsivity of 2.5×10^{-5} A/W is comparable to values previously reported, e.g. 3.5 mA/W for plasmonic photocurrent stimulated by Au nanoislands on silicon substrate by Nazirzadeh et al. [51] and 0.6 mA/W by periodic gold gratings on silicon by Sobhani et al.[52]. Plasmonic photocurrent was also observed in other different device structures utilizing Au nanoislands as a broadband absorbers [53,54,24].

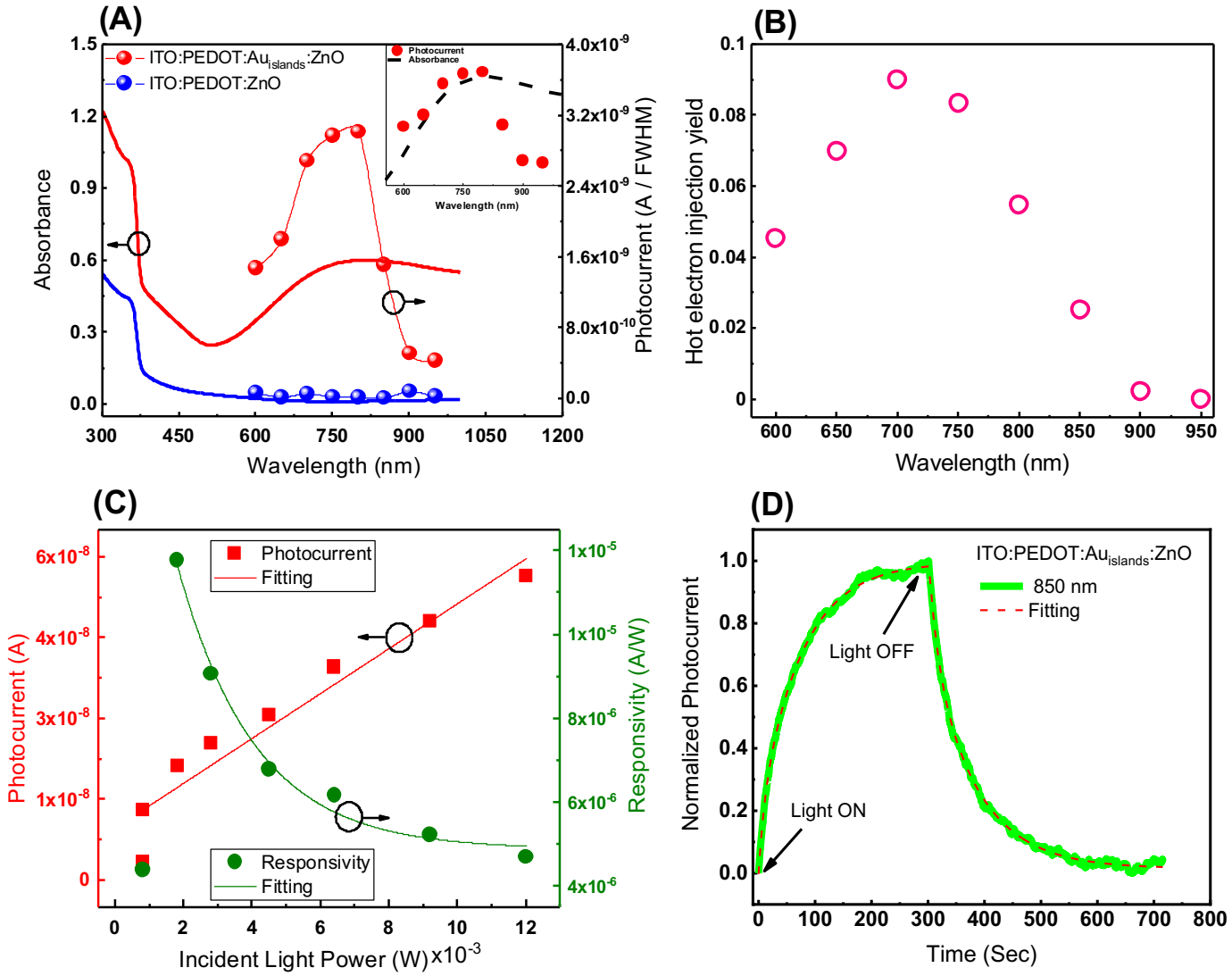

Figure 3: Shows (A) The absorption spectrum of the investigated devices combined with their photocurrent data measured at different wavelengths using bandpass filters. The photocurrent data were corrected with the bandpass FWHM. The inset shows a magnification to the normalized plasmonic photocurrent and absorption of the plasmonic device in the NIR. (B) The hot electron injection yield calculated by multiplying Fowler's equation with the plasmonic absorption of Au nanoislands. Each point is averaged over the spectral bandwidth of the notch filters used in the experiment to enable a direct comparison with the experimental results. (C) The recorded photocurrent and responsivity at 850 nm as a function of incident power as shown in the supplementary figure S4. Neutral density filters were used to adjust the light power to the desired values. (D) The fitted photocurrent transient of the plasmonic device irradiated at 850 nm for 5 minutes with 10 mV bias applied across the device.

Mechanism of photocurrent generation

Improving optical absorption is an important step towards an effective photocurrent generation. In this work, the ordinary ZnO absorption was spectrally extended through the plasmonic resonances of Au nanoislands, with the observed persistent photocurrent in the near-IR a direct consequence of the plasmonic generation of hot charge carriers in the Au nanoislands. Additionally, the large interface area of the Schottky barrier between the Au nanostructures and the ZnO NPs layer enables the efficient separation of the plasmonically generated hot electrons necessary for the generation of a photocurrent [55].

To get further insight into the hot charge carriers injection mechanism, the time evolution of the plasmonic device photoresponse was recorded, with the device illuminated at a wavelength of 850 nm (probing the plasmonic hot charge carrier generation from the Au nanoislands) for 5 minutes and in the dark for the following 5 minutes (Figure 3D). Fitting of the transient photocurrent curve yields the time constants of the plasmonic device and can best be described by using a double exponential function with two different time constants (τ_1 and τ_2) for the rise [$y = y_\circ + A_1 e^{(x/\tau_1)} + A_2 e^{(x/\tau_2)}$] and decay [$y = y_\circ + A_1 e^{(-x/\tau_1)} + A_2 e^{(-x/\tau_2)}$] photocurrent responses respectively. As the device is illuminated, the resulting photocurrent shows two timescale components; a fast rise component (τ_1) with time constant of 9.5 sec followed by a slow photocurrent evolution with time constant (τ_2) of 73.5 sec. When the illumination is switched off, photocurrent also shows a fast and slow decay time constant of 15.5 sec and 81.7 sec respectively.

Despite having its origin in plasmonically mediated hot charge carriers, the near-IR photocurrent observed here displays slower time constants compared to what is normally reported for this mechanism [56,57,58]. In fact, the timescales observed are consistent with the persistent photoconductivity in ZnO NPs, attributed to the polycrystalline nature of ZnO and the inherited surface trap states which facilitate the quality of the established junction interface with the Au nanostructures [59,60]. Additionally, the reduction of the Schottky barrier as a result of charge trapping in ZnO surface defects results in an increase in PC after trap saturation [59]. Indeed, the incorporation of plasmonic metal nanoparticles with metal oxides was shown to increase the oxygen vacancy defects concentration and create shallow charge traps which improve charge transportation across the metal nanoparticles-semiconductor interface [61]. Consequently, we propose that the observed large enhancement in NIR photocurrent, accompanied with slow rise

and decay times well below the bandgap energy of ZnO, is attributed to hot electrons injected into surface defect traps by tunnelling through the Schottky barrier leading to trap saturation and hence slow time constants. The coupling between localized surface plasmons and the defect states in the surrounding medium is also supported by other research groups like Hwang et al. [62] and Lian et al. [47].

4- Conclusion

In summary, a solution processed photodetector based on ZnO nanoparticles was demonstrated for the visible to near-IR wavelength range by capitalising on the plasmonically generated hot charge carriers of Au nanoislands. In addition to maintaining charge balance, Au evaporation onto the PEDOT:PSS layer allowed for the formation of nanoisland structures without the need for temperature annealing. The resulting plasmonically enhanced ZnO photodetector device exhibits a photoresponse in the visible-NIR range of 2.5×10^{-5} A/W, therefore providing a route to solution processed, low-cost device fabrication schemes with important implications on low processing temperature optoelectronics technology to enhance the performance of photovoltaic devices over a wide solar spectrum. Additionally, the persistent nature of the observed photocurrent indicates the significant role of surface defects electrons in the photocurrent dynamics, opening the route for the development of new techniques in probing surface defects.

Supplementary Material

See supplementary material for more details on the plasmonic working device and its I-V characteristics. The file also shows the recorded responsivity transient as a function of wavelength.

References

(1) Dauzon, E.; Sallenave, X.; Plesse, C.; Goubard, F.; Amassian, A.; Anthopoulos, T. D. Pushing the Limits of Flexibility and Stretchability of Solar Cells: A Review. *Adv. Mater.* **2021**, *33*, 2101469. https://doi.org/10.1002/adma.202101469.

(2) Yu, X.; Marks, T. J.; Facchetti, A. Metal Oxides for Optoelectronic Applications. *Nat. Mater.* **2016**, *15* (4), 383–396. https://doi.org/10.1038/nmat4599.

(3) Ouyang, W.; Chen, J.; Shi, Z.; Fang, X. Self-Powered UV Photodetectors Based on ZnO Nanomaterials. *Appl. Phys. Rev.* **2021**, *8* (3), 031315. https://doi.org/10.1063/5.0058482.

(4) Chen, Y.; Su, L.; Jiang, M.; Fang, X. Switch Type PANI/ZnO Core-Shell Microwire Heterojunction for UV Photodetection. *J. Mater. Sci. Technol.* **2022**, *105*, 259–265. https://doi.org/10.1016/j.jmst.2021.07.031.

(5) Ibrahem, M. A.; Verrelli, E.; Lai, K. T.; Kyriakou, G.; Lee, A. F.; Isaacs, M. A.; Cheng, F.; O'Neill, M. Dual Wavelength (Ultraviolet and Green) Photodetectors Using Solution Processed Zinc Oxide Nanoparticles. *ACS Appl. Mater. Interfaces* **2017**, *9* (42), 36971–36979. https://doi.org/10.1021/acsami.7b08092.

(6) Campbell, J. C. Recent Advances in Telecommunications Avalanche Photodiodes. *J. Light. Technol.* **2007**, *25* (1), 109–121. https://doi.org/10.1109/JLT.2006.888481.

(7) Blanco, M.; Villarroya, I. NIR Spectroscopy: A Rapid-Response Analytical Tool. *TrAC Trends Anal. Chem.* **2002**, *21* (4), 240–250. https://doi.org/10.1016/S0165-9936(02)00404-1.

(8) Hansen, M. P.; Malchow, D. S. Overview of SWIR Detectors, Cameras, and Applications; Vavilov, V. P., Burleigh, D. D., Eds.; SPIE Defense and Security Symposium. International Society for Optics and Photonics, 2008; p 69390I. https://doi.org/10.1117/12.777776.

(9) Zhong, Y.; Wasserman, D.; Zhong, Y.; Malagari, S. D.; Hamilton, T.; Wasserman, D. Review of Mid-Infrared Plasmonic Materials Review of Mid-Infrared Plasmonic Materials. *J. Nanophotonics* **2015**, *9*, 093791. https://doi.org/10.1117/1.JNP.9.093791.

(10) Luo, L.-B.; Chen, J.-J.; Wang, M.-Z.; Hu, H.; Wu, C.-Y.; Li, Q.; Wang, L.; Huang, J.-A.; Liang, F.-X. Near-Infrared Light Photovoltaic Detector Based on GaAs Nanocone Array/Monolayer Graphene Schottky Junction. *Adv. Funct. Mater.* **2014**, *24* (19), 2794–2800. https://doi.org/10.1002/adfm.201303368.

(11) Li, C.; Huang, W.; Gao, L.; Wang, H.; Hu, L.; Chen, T.; Zhang, H. Recent Advances in Solution-Processed Photodetectors Based on Inorganic and Hybrid Photo-Active Materials. *Nanoscale* **2020**, *12* (4), 2201–2227. https://doi.org/10.1039/C9NR07799E.

(12) García de Arquer, F. P.; Armin, A.; Meredith, P.; Sargent, E. H. Solution-Processed Semiconductors for next-Generation Photodetectors. *Nat. Rev. Mater.* **2017**, *2* (3), 16100. https://doi.org/10.1038/natrevmats.2016.100.

(13) Yuan, Z.; Wang, W.; Wu, H.; Nie, F.; He, J. A Solution-Processed ZnO Quantum Dots Ultraviolet Photodetector with High Performance Driven by Low Operating Voltage. *Mater. Lett.* **2020**, *278*, 128413. https://doi.org/10.1016/j.matlet.2020.128413.

(14) Zhang, Y.; Xu, J.; Shi, S.; Gao, Y.; Wang, C.; Zhang, X.; Yin, S.; Li, L. Development of Solution-Processed ZnO Nanorod Arrays Based Photodetectors and the Improvement of UV Photoresponse via AZO Seed Layers. *ACS Appl. Mater. Interfaces* **2016**, *8* (34), 22647–22657. https://doi.org/10.1021/acsami.6b06700.

(15) Ibrahem, M. A.; Verrelli, E.; Lai, K. T.; Kyriakou, G.; Lee, A. F.; Isaacs, M. A.; Cheng, F.; O'Neill, M. Dual Wavelength (Ultraviolet and Green) Photodetectors Using Solution Processed Zinc Oxide Nanoparticles. *ACS Appl. Mater. Interfaces* **2017**, *9* (42), 36971–36979. https://doi.org/10.1021/acsami.7b08092.

(16) Zhou, H.; Fang, G.; Yuan, L.; Wang, C.; Yang, X.; Huang, H.; Zhou, C.; Zhao, X. Deep Ultraviolet and near Infrared Photodiode Based on N-ZnO/p -Silicon Nanowire Heterojunction Fabricated at Low Temperature. *Appl. Phys. Lett.* **2009**, *94* (1). https://doi.org/10.1063/1.3064161.

(17) Cheng, B.; Xu, J.; Ouyang, Z.; Xie, C.; Su, X.; Xiao, Y.; Lei, S. Individual ZnO Nanowires for

Photodetectors with Wide Response Range from Solar-Blind Ultraviolet to near-Infrared Modulated by Bias Voltage and Illumination Intensity. *Opt. Express* **2013**, *21* (24), 29719. https://doi.org/10.1364/OE.21.029719.

(18) Liu, H.; Sun, Q.; Xing, J.; Zheng, Z.; Zhang, Z.; Lü, Z.; Zhao, K. Fast and Enhanced Broadband Photoresponse of a ZnO Nanowire Array/Reduced Graphene Oxide Film Hybrid Photodetector from the Visible to the near-Infrared Range. *ACS Appl. Mater. Interfaces* **2015**, *7* (12), 6645–6651. https://doi.org/10.1021/am509084r.

(19) Liu, H.; Zhang, X.; Zhang, L.; Yin, Z.; Wang, D.; Meng, J.; Jiang, Q.; Wang, Y.; You, J. A High-Performance Photodetector Based on an Inorganic Perovskite–ZnO Heterostructure. *J. Mater. Chem. C* **2017**, *5* (25), 6115–6122. https://doi.org/10.1039/C7TC01998J.

(20) Li, J.; Cushing, S. K.; Meng, F.; Senty, T. R.; Bristow, A. D.; Wu, N. Plasmon-Induced Resonance Energy Transfer for Solar Energy Conversion. *Nat. Photonics* **2015**, *9* (9), 601–607. https://doi.org/10.1038/nphoton.2015.142.

(21) Shaik, F.; Peer, I.; Jain, P. K.; Amirav, L. Plasmon-Enhanced Multicarrier Photocatalysis. *Nano Lett.* **2018**, *18* (7), 4370–4376. https://doi.org/10.1021/acs.nanolett.8b01392.

(22) Chen, H.; Su, L.; Jiang, M.; Fang, X. Highly Desirable Photodetectors Derived from Versatile Plasmonic Nanostructures. *Adv. Funct. Mater.* **2017**, *27* (45), 1704181. https://doi.org/10.1002/adfm.201704181.

(23) Knight, M. W.; Sobhani, H.; Nordlander, P.; Halas, N. J. Photodetection with Active Optical Antennas. *Science (80-.).* **2011**, *332* (6030), 702–704. https://doi.org/10.1126/science.1203056.

(24) Wenyi Wang, Andrey Klots, Dhiraj Prasai, Yuanmu Yang, Kirill I. Bolotin, and J. V. Hot Electron-Based Near-Infrared Photodetection Using Bilayer MoS 2anmu Yang, Kirill I. Bolotin, and Jason Valentine. *Nano Lett.* **2015**, *15* (11), 7440–7444. https://doi.org/10.1021/acs.nanolett.5b02866.

(25) Wu, X.; Centeno, A.; Zhang, X.; Darvill, D.; Ryan, M. P.; Riley, D. J.; Alford, N. M.; Xie, F. Broadband Plasmon Photocurrent Generation from Au Nanoparticles/ Mesoporous TiO2 Nanotube Electrodes. *Sol. Energy Mater. Sol. Cells* **2015**, *138*, 80–85. https://doi.org/10.1016/j.solmat.2015.02.021.

(26) Shi, X.; Ueno, K.; Oshikiri, T.; Misawa, H. Improvement of Plasmon-Enhanced Photocurrent Generation by Interference of TiO 2 Thin Film. *J. Phys. Chem. C* **2013**, *117* (47), 24733–24739. https://doi.org/10.1021/jp408472g.

(27) Furube, A.; Du, L.; Hara, K.; Katoh, R.; Tachiya, M. Ultrafast Plasmon-Induced Electron Transfer from Gold Nanodots into TiO 2 Nanoparticles. *J. Am. Chem. Soc.* **2007**, *129* (48), 14852–14853. https://doi.org/10.1021/ja076134v.

(28) Gaspar, D.; Pimentel, A. C.; Mateus, T.; Leitão, J. P.; Soares, J.; Falcão, B. P.; Araújo, A.; Vicente, A.; Filonovich, S. A.; Águas, H.; et al. Influence of the Layer Thickness in Plasmonic Gold Nanoparticles Produced by Thermal Evaporation. *Sci. Rep.* **2013**, *3* (1), 1469. https://doi.org/10.1038/srep01469.

(29) Serrano, A.; De La Fuente, O. R.; García, M. A. Extended and Localized Surface Plasmons in Annealed Au Films on Glass Substrates. *J. Appl. Phys.* **2010**, *108* (7).

https://doi.org/10.1063/1.3485825.

(30) Piscopiello, E.; Tapfer, L.; Antisari, M. V.; Paiano, P.; Prete, P.; Lovergine, N. Formation of Epitaxial Gold Nanoislands on (100) Silicon. *Phys. Rev. B* **2008**, *78* (3), 035305. https://doi.org/10.1103/PhysRevB.78.035305.

(31) Ibrahem, M.; Verrelli, E.; Lai, K.; Kyriakou, G.; Lee, A.; Isaacs, M.; Cheng, F.; O'Neill, M. Dual Wavelength (Ultraviolet and Green) Photodetectors Using Solution Processed Zinc Oxide Nanoparticles. *ACS Appl. Mater. Interfaces 9* (42), 36971–36979. https://doi.org/10.1021/acsami.7b08092.

(32) Ruffino, F.; Grimaldi, M. G. Atomic Force Microscopy Study of the Growth Mechanisms of Nanostructured Sputtered Au Film on Si(111): Evolution with Film Thickness and Annealing Time. *J. Appl. Phys.* **2010**, *107* (10), 104321. https://doi.org/10.1063/1.3428467.

(33) Verrelli, E.; Michelakaki, I.; Boukos, N.; Kyriakou, G.; Tsoukalas, D. Coalescence of Cluster Beam Generated Sub-2 Nm Bare Au Nanoparticles and Analysis of Au Film Growth Parameters. *Ann. Phys.* **2018**, *530* (2), 1–13. https://doi.org/10.1002/andp.201700256.

(34) Lang, U.; Muller, E.; Naujoks, N.; Dual, J. Microscopical Investigations of PEDOT:PSS Thin Films. *Adv. Funct. Mater.* **2009**, *19* (8), 1215–1220. https://doi.org/10.1002/adfm.200801258.

(35) Leosson, K.; Ingason, A. S.; Agnarsson, B.; Kossoy, A.; Olafsson, S.; Gather, M. C. Ultra-Thin Gold Films on Transparent Polymers. *Nanophotonics* **2013**, *2* (1), 3–11. https://doi.org/10.1515/nanoph-2012-0030.

(36) Ibrahem, M. A.; Rasheed, B. G.; Mahdi, R. I.; Khazal, T. M.; Omar, M. M.; O'Neill, M. Plasmonic-Enhanced Photocatalysis Reactions Using Gold Nanostructured Films. *RSC Adv.* **2020**, *10* (38), 22324–22330. https://doi.org/10.1039/d0ra03858j.

(37) Ooms, M. D.; Jeyaram, Y.; Sinton, D. Disposable Plasmonics: Rapid and Inexpensive Large Area Patterning of Plasmonic Structures with CO 2 Laser Annealing. *Langmuir* **2015**, *31* (18), 5252–5258. https://doi.org/10.1021/acs.langmuir.5b01092.

(38) Jin, Y.; Wang, J.; Sun, B.; Blakesley, J. C.; Greenham, N. C. Solution-Processed Ultraviolet Photodetectors Based on Colloidal ZnO Nanoparticles. *Nano Lett.* **2008**, *8* (6), 1649–1653. https://doi.org/10.1021/nl0803702.

(39) Gu, S.; Neugebauer, H.; Sariciftci, N. S. Conjugated Polymer-Based Organic Solar Cells. **2007**, *107*, 1324–1338. https://doi.org/10.1021/cr050149z.

(40) Lin, P.; Yan, X.; Zhang, Z.; Shen, Y.; Zhao, Y.; Bai, Z.; Zhang, Y. Self-Powered UV Photosensor Based on PEDOT:PSS/ZnO Micro/Nanowire with Strain-Modulated Photoresponse. *ACS Appl. Mater. Interfaces* **2013**, *5* (9), 3671–3676. https://doi.org/10.1021/am4008775.

(41) Sessolo, M.; Bolink, H. J. Hybrid Organic-Inorganic Light-Emitting Diodes. *Adv. Mater.* **2011**, *23* (16), 1829–1845. https://doi.org/10.1002/adma.201004324.

(42) Fowler, R. H. The Analysis of Photoelectric Sensitivity Curves for Clean Metals at Various Temperatures. *Phys. Rev.* **1931**, *38* (1), 45–56. https://doi.org/10.1103/PhysRev.38.45.

(43) Ouyang, W.; Teng, F.; Jiang, M.; Fang, X. ZnO Film UV Photodetector with Enhanced Performance: Heterojunction with CdMoO 4 Microplates and the Hot Electron Injection Effect of Au Nanoparticles. *Small* **2017**, *13* (39), 1702177. https://doi.org/10.1002/smll.201702177.

(44) Lee, H.; Song, K.; Lee, M.; Park, J. Y. In Situ Visualization of Localized Surface Plasmon Resonance-Driven Hot Hole Flux. *Adv. Sci.* **2020**, *7* (20), 2001148. https://doi.org/10.1002/advs.202001148.

(45) Yan, T.; Cai, S.; Hu, Z.; Li, Z.; Fang, X. Ultrafast Speed, Dark Current Suppression, and Self-Powered Enhancement in TiO 2 -Based Ultraviolet Photodetectors by Organic Layers and Ag Nanowires Regulation. *J. Phys. Chem. Lett.* **2021**, *12* (40), 9912–9918. https://doi.org/10.1021/acs.jpclett.1c03090.

(46) Giugni, A.; Torre, B.; Toma, A.; Francardi, M.; Malerba, M.; Alabastri, A.; Proietti Zaccaria, R.; Stockman, M. I.; Di Fabrizio, E. Hot-Electron Nanoscopy Using Adiabatic Compression of Surface Plasmons. *Nat. Nanotechnol.* **2013**, *8* (11), 845–852. https://doi.org/10.1038/nnano.2013.207.

(47) Wu, K.; Chen, J.; McBride, J. R.; Lian, T. Efficient Hot-Electron Transfer by a Plasmon-Induced Interfacial Charge-Transfer Transition. *Science (80-.).* **2015**, *349* (6248), 632–635. https://doi.org/10.1126/science.aac5443.

(48) Raji, R.; Gopchandran, K. G. Plasmonic Photocatalytic Activity of ZnO:Au Nanostructures: Tailoring the Plasmon Absorption and Interfacial Charge Transfer Mechanism. *J. Hazard. Mater.* **2019**, *368*, 345–357. https://doi.org/10.1016/j.jhazmat.2019.01.052.

(49) Lee, S. J.; Kim, J.-Y.; Mohd Yusoff, A. R. bin; Jang, J. Plasmonic Organic Solar Cell Employing Au NP:PEDOT:PSS Doped RGO. *RSC Adv.* **2015**, *5* (30), 23892–23899. https://doi.org/10.1039/C5RA02878G.

(50) Liu, D.; Yang, D.; Gao, Y.; Ma, J.; Long, R.; Wang, C.; Xiong, Y. Flexible Near-Infrared Photovoltaic Devices Based on Plasmonic Hot-Electron Injection into Silicon Nanowire Arrays. *Angew. Chemie Int. Ed.* **2016**, *55* (14), 4577–4581. https://doi.org/10.1002/anie.201600279.

(51) Nazirzadeh, M. A.; Atar, F. B.; Turgut, B. B.; Okyay, A. K. Random Sized Plasmonic Nanoantennas on Silicon for Low-Cost Broad-Band near-Infrared Photodetection. *Sci. Rep.* **2015**, *4* (1), 7103. https://doi.org/10.1038/srep07103.

(52) Sobhani, A.; Knight, M. W.; Wang, Y.; Zheng, B.; King, N. S.; Brown, L. V.; Fang, Z.; Nordlander, P.; Halas, N. J. Narrowband Photodetection in the Near-Infrared with a Plasmon-Induced Hot Electron Device. *Nat. Commun.* **2013**, *4*, 1643. https://doi.org/10.1038/ncomms2642.

(53) Tan, F.; Li, T.; Wang, N.; Lai, S. K.; Tsoi, C. C.; Yu, W.; Zhang, X. Rough Gold Films as Broadband Absorbers for Plasmonic Enhancement of TiO2 Photocurrent over 400–800 Nm. *Sci. Rep.* **2016**, *6* (April), 33049. https://doi.org/10.1038/srep33049.

(54) Sharma, A.; Kumar, R.; Bhattacharyya, B.; Husale, S. Hot Electron Induced NIR Detection in CdS Films. *Sci. Rep.* **2016**, *6* (November 2015), 1–6. https://doi.org/10.1038/srep22939.

(55) Hu, K.; Chen, H.; Jiang, M.; Teng, F.; Zheng, L.; Fang, X. Broadband Photoresponse Enhancement of a High-Performance t -Se Microtube Photodetector by Plasmonic Metallic Nanoparticles. *Adv. Funct. Mater.* **2016**, *26* (36), 6641–6648. https://doi.org/10.1002/adfm.201602408.

(56) Lee, Y. K.; Jung, C. H.; Park, J.; Seo, H.; Somorjai, G. A.; Park, J. Y. Surface Plasmon-Driven Hot Electron Flow Probed with Metal-Semiconductor Nanodiodes. *Nano Lett.* **2011**, *11* (10), 4251–4255. https://doi.org/10.1021/nl2022459.

(57) Lee, H.; Lee, Y. K.; Hwang, E.; Park, J. Y. Enhanced Surface Plasmon Effect of Ag/TiO 2 Nanodiodes on Internal Photoemission. *J. Phys. Chem. C* **2014**, *118* (11), 5650–5656. https://doi.org/10.1021/jp409894b.

(58) Clavero, C. Plasmon-Induced Hot-Electron Generation at Nanoparticle/Metal-Oxide Interfaces for Photovoltaic and Photocatalytic Devices. *Nat. Photonics* **2014**, *8* (2), 95–103. https://doi.org/10.1038/nphoton.2013.238.

(59) Andrea Pescaglini, Alfonso Martín, Davide Cammi, Gediminas Juska, Carsten Ronning, E. P.; and Daniela Iacopino. Hot-Electron Injection in Au Nanorod–ZnO Nanowire Hybrid Device for Near-Infrared Photodetection. *Nano Lett.* **2014**, *14* (11), 6202–6209. https://doi.org/10.1021/nl5024854.

(60) Lee, H.; Lee, H.; Park, J. Y. Direct Imaging of Surface Plasmon-Driven Hot Electron Flux on the Au Nanoprism/TiO 2. *Nano Lett.* **2019**, *19* (2), 891–896. https://doi.org/10.1021/acs.nanolett.8b04119.

(61) Paul, K. K.; Giri, P. K. Role of Surface Plasmons and Hot Electrons on the Multi-Step Photocatalytic Decay by Defect Enriched Ag@TiO2Nanorods under Visible Light. *J. Phys. Chem. C* **2017**, *121* (36), 20016–20030. https://doi.org/10.1021/acs.jpcc.7b05328.

(62) Hwang, J. D.; Wang, F. H.; Kung, C. Y.; Lai, M. J.; Chan, M. C. Annealing Effects of Au Nanoparticles on the Surface-Plasmon Enhanced p-Si/n-ZnO Nanorods Heterojunction Photodetectors. *J. Appl. Phys.* **2014**, *115* (17), 173110. https://doi.org/10.1063/1.4875657.